Interferometric technique for engineering indistinguishability and entanglement of photon pairs

David Branning*

Optical Technology Division, NIST, Gaithersburg, Maryland 20899-8441

Warren Grice[†]

Department of Physics, Southern Illinois University, Edwardsville, Illinois 62026

Reinhard Erdmann[†]

Air Force Research Laboratory, SNDP, Rome, New York 13441

I. A. Walmsley

The Institute of Optics, University of Rochester, Rochester, New York 14627

We give a detailed account of a recently introduced technique to suppress distinguishing information in the space-time component of the state vector of a pair of photons. The method works by creating interference between two possible ways for each photon to occupy any given space-time mode. Under certain conditions, this technique also allows the preparation of the two photons in a highly entangled space-time state.

PACS number(s): 42.50.Ar, 03.65.Bz

INTRODUCTION

From the beginnings of quantum theory, entanglement has proved to be its most distinctive and puzzling feature. Entangled states are central to our understanding of quantum measurement and complementarity, due to the famous efforts of Einstein, Bohr, Von Neumann, Bell, and many others, to firmly establish these concepts [1]. In the latter half of this century, entangled particles have been and continue to be used in a wide variety of experiments that demonstrate nature's nonclassical or nonlocal behavior. Such experiments have been performed to clarify our intuitions about complementarity [2,3], or to test quantum mechanics against more ''complete'' rival theories of local hidden variables [4–6].

In recent years, though, entanglement has come to be viewed not only as the source of our philosophical difficulties with quantum theory, but also as a resource for emerging information processing technologies such as quantum cryptography, quantum dense coding, quantum teleportation, and quantum computing [7]. Additionally, entanglement and quantum interference effects have been put to good use in the field of optical metrology, where they have enabled absolute measurements of radiance, photodetector efficiencies, and birefringence of optical media [8].

For almost all of these applications, the most convenient and luminous source of entangled particles is the spontaneous parametric downconverter (SPDC), which converts a small fraction of incident ''pump'' photons into pairs of ''signal'' and ''idler'' photons whose energies, momenta, and emission times are automatically entangled [9] if the pump is monochromatic. Additionally, the polarizations of

the signal and idler photons may become entangled if two distinct pair-creation events with orthogonally polarized emissions[1] are made to interfere with each other [10,11]. According to the rules of quantum mechanics [12], this interference is allowed only when the two creation events are indistinguishable in principle by any ancillary measurements of momentum, energy, etc. Therefore, effective polarization entanglement requires the suppression of any distinguishing information in the space-time portion of the photons' state vector.

One way of determining the existence of such distinguishing information is via the Hong-Ou-Mandel (HOM) interferometer [13], in which two photons are coincident simultaneously on different input ports of a 50/50 beamsplitter and the output ports are monitored in coincidence by a pair of photon-counting detectors. If the signal and idler photons are indistinguishable at the detectors, so that it is impossible to determine which photon arrived at each detector, a remarkable thing happens: they do not generate coincidence counts. This occurs because the amplitudes for the two processes that lead to a coincidence count (double reflection or double transmission at the beamsplitter) have opposite signs, and therefore cancel each other when superposed. If, on the other hand, the signal and idler are distinguishable from one another in any way—say, by relative time of arrival—then the destructive interference does not occur. Thus, the coincidence counting rate at the interference null in a HOM interferometer is a direct measure of the intrinsic distinguishability of the signal and idler photons.

Recently, states with more than two entangled photons have been generated for the purposes of quantum teleportation [14], entanglement swapping [15], and the Greenberger-

---

*Author was at the Department of Physics and Astronomy, University of Rochester, for this work.

[†]Authors were at the Institute of Optics, University of Rochester, for this work.

[1]The signal and idler photons need not be polarized orthogonally to *each other* in these schemes, but only to their signal or idler counterparts from the second PDC process.

Horne-Zeilinger test of nonlocality [16]. These states were created using the synchronized emission from two type-II downconverters that were pumped not by a monochromatic beam but by a train of ultrashort (200 fs) pulses. It is becoming clear [17] that such ultrashort pulse-pumped sources, with their potential for multisource synchronization, will be critical in many applications of quantum entanglement for information processing.

Unfortunately, it is also clear that ultrashort pulse pumping of type-II media results in the presence of distinguishing information in the time-frequency (or ''chronocyclic'' [18]) domain; that is, the signal and idler photons that emerge from such a source may have different spectral distributions, or different emission-time distributions, from one another. Thus they are no longer as chronocyclically indistinguishable, and therefore as polarization entangleable, as the photon pairs that emerge from a cw-pumped downconverter at random times. The presence of this distinguishing chronocyclic information for pulse-pumped type-II downconversion has already been established theoretically [19,20] and experimentally [21,22].

The solution to this problem that is usually adopted is to impose severe spectral filtering on the signal and idler photons, so that the most spectrally indistinguishable subset of the pairs is selected. The counting rates in such experiments are reduced accordingly. Very recently, however, we reported on a method of suppressing this distinguishing space-time information at the source [23], so that such filters are no longer necessary.

In this paper, we will analyze the method in full detail. We will also present experimental data from a HOM interferometer that show that this technique can suppress the distinguishing time-frequency information for the two photons. Additionally, we will show that, in some cases, this technique can directly enhance entanglement in the time-frequency domain, or even create it where none existed before.

PRINCIPLE OF THE METHOD

In its most general form, the quantum state describing a pair of signal and idler photons emitted by a downconverter is

$$|\psi\rangle = \int \int dx\, dy\, f(x,y)|x\rangle|y\rangle, \qquad (1)$$

where $|x\rangle$ ($|y\rangle$) denotes a single-photon Fock state in mode x (y). Here x and y are mode labels that refer to propagation direction, frequency (or time), and polarization: $x = (\omega_s, \vec{x})$ and $y = (\omega_i, \vec{y})$, where $\vec{x}$ and $\vec{y}$ are transverse polarization vectors and ω_s (ω_i) is the frequency of the signal (idler) photon. The state (1) is entangled if the joint emission amplitude function $f(x,y)$ is not factorable into a product of the form $g(x)h(y)$. If the function is nonfactorable only for a subset of the degrees of freedom represented by x (y), e.g., if $f(\omega_s, \omega_i) \neq g(\omega_s)h(\omega_i)$, then entanglement exists only for that subset.

As mentioned in the Introduction, one way of creating entanglement is to coherently superpose two distinct pair-creation processes, so that the two-photon state consists of a superposition of the amplitudes generated by each process. For example, suppose that initially the joint amplitude function in Eq. (1) factors according to

$$f(x,y) = g(x)h(y). \qquad (2)$$

Then the state $|\psi\rangle$ is unentangled, since it may easily be written as a product of states in distinct Hilbert spaces for each particle. However, the superposition state

$$|\Psi\rangle = \int \int dx\, dy[f(x,y) + e^{i\theta}f(y,x)]|x\rangle|y\rangle \qquad (3)$$

will be highly entangled, provided $g(x)h(y) \neq g(y)h(x)$, i.e., the joint amplitude function is not symmetric with respect to interchange of its arguments. In fact, the most entangled state occurs if either of these products is zero for some $\{x,y\}$ while the other is not, since then the combination $\lfloor g(x)h(y) + e^{i\theta}g(y)h(x) \rfloor$ is, for certain values of θ, farthest from being a factorable function (see Fig. 1). This is discussed quantitatively in a forthcoming paper [24].

Another consequence of this procedure is that for certain values of θ, the joint amplitude function in Eq. (3) becomes

$$f'(x,y) = f(x,y) + f(y,x), \qquad (4)$$

which is symmetric under exchange of x and y by definition, regardless of the symmetry properties of $f(x,y)$. It turns out that this kind of exchange symmetry is a requirement for maintaining the chronocyclic indistinguishability of the photons, because the degree of two-photon interference in a HOM interferometer depends on the symmetry of the joint emission amplitude spectrum [19]. That is, for photons entering a HOM interferometer with emission spectrum $f(\omega_s, \omega_i)$, complete destructive interference can only occur when

$$f(\omega_s, \omega_i) = f(\omega_i, \omega_s) \qquad (5)$$

over the range of detected frequencies [22]. The symmetry in Eq. (5) ensures that it is impossible to use the pair of detected photon frequencies as a ''marker'' indicating which photon went to which detector, so that interference can occur.

Therefore, the creating of entanglement via Eq. (3) also has the effect of suppressing distinguishing information at the source, by directly symmetrizing the entire joint emission amplitude spectrum. To implement this method, we must add together two downconversion processes: one governed by $f(\omega_s, \omega_i)$, the other, with the signal and idler polarizations exchanged, governed by $f(\omega_i, \omega_s)$. The emission from such a system is then governed by a new joint amplitude emission spectrum that is guaranteed to be symmetric:

$$f'(\omega_s, \omega_i) = f(\omega_s, \omega_i) + f(\omega_i, \omega_s). \qquad (6)$$

To experimentally realize the amplitude addition in Eq. (6), we must add the second process to the first one *coherently*,
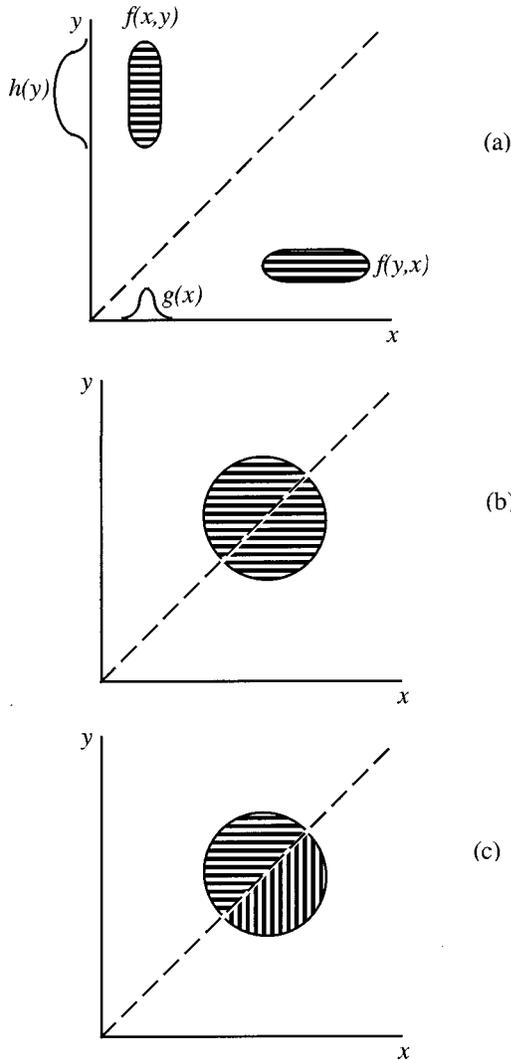
FIG. 1. (a) The joint amplitude function $f(x,y)$ may be factored into a product of marginal distributions $g(x)$ and $h(y)$, implying that $|\psi\rangle$ in Eq. (1) is an unentangled product state. However, if the amplitude $f(y,x)$ is added, the resulting amplitude cannot be written as a product of marginal distributions, so that $|\Psi\rangle$ in Eq. (3) is entangled. In some cases, the degree of entanglement can depend on the relative phase between $f(x,y)$ and $f(y,x)$; for example, when the amplitude functions in (b) are added together, the resulting function is actually less entangled than $f(x,y)$ or $f(y,x)$. However, if they are subtracted (c), the resulting function is at least as entangled as $f(x,y)$ or $f(y,x)$. Horizontal lines indicate positive-valued functions, while vertical lines indicate negative-valued functions.

so that it is impossible in principle to distinguish which of the two downconversion processes generates each photon pair [25].

Since the presence of HOM interference is a good test for the symmetry of $f'(\omega_s,\omega_i)$, we expect that the photons carrying a joint amplitude emission spectrum of the symmetrized form (6) will produce a good HOM interference null in the coincidence counting rate, regardless of the initial symmetry properties of $f(\omega_s,\omega_i)$. The HOM null is always a clear sign of path indistinguishability for the photon pairs,

but in this case it is also a sign that entanglement has been created, provided $f(\omega_s,\omega_i)$ fails to satisfy Eq. (5). This is the case when a type-II SPDC is pumped by an ultrashort pulse whose bandwidth is comparable to that of the crystal phase-matching function. Therefore, our experiment consists of constructing a symmetrized source and then looking for a lower minimum in the HOM coincidence ''dip'' as a sign that the superposition—and consequently, the entanglement—was successfully carried out.

EXPERIMENTAL ARRANGEMENT

The coherent addition in Eq. (6) may be accomplished experimentally with the apparatus shown in Fig. 2. An ultrafast pump source for the spontaneous downconversion process is created by frequency-doubling the output of a mode-locked Ti:sapphire oscillator. The frequency-doubled pulses are separated from the residual fundamental by means of a dispersion-compensated prism sequence. Each pump pulse enters the parametric downconverter (PDC) from the left, possibly creating an orthogonally polarized, frequency degenerate pair of photons somewhere inside. After exiting the PDC, the pump is reflected by a dichroic mirror (MD2), while the lower-wavelength downconverted light is transmitted through it. The pump is normally incident on a mirror (M1) that reflects it back into the PDC. The signal and idler, meanwhile, are sent through a λ/4 plate and then onto a mirror (M2) at normal incidence. They are then reflected back through the λ/4 plate and into the PDC, overlapping with the pump pulse in the center of the crystal.

The λ/4 plate is oriented with its optical axis at 45° to the ''o'' and ''e'' axes of the PDC. After two passes through this plate, both the signal and idler polarizations are rotated through 90°, effectively exchanging their roles as the e- and o-polarized photons. As a result, the e-polarized light that is sent back into the downconverter actually carries the spectrum belonging to the original o polarization, and vice versa; more generally, the joint emission amplitude spectrum for these pairs is switched from $f(\omega_o,\omega_e)$ to $f(\omega_e,\omega_o)$. This exchange also has the effect of canceling the temporal walkoff for photon pairs emitted from the center of the crystal: the photon with the fast o polarization on the way out has the slow e polarization on the way back in. Some additional, uncompensated walkoff then occurs for all the photons as they travel from the center of the crystal to the final output face.

This system functions as a Michelson interferometer, with the dichroic mirror MD2 playing the role of the central beamsplitter, separating and recombining the ''signal and idler'' arm of the downconversion and the ''pump'' arm. Unlike a traditional Michelson interferometer, the interfering pathways here do not begin and end at the beamsplitter; they do so within the PDC. With the arms properly aligned, and with their optical path lengths balanced to within the coherence time of the pump, it becomes impossible in principle to discern whether the downconverted light that ultimately emerges from the PDC is generated from the first or the second pass of the pump pulse through the crystal. The resulting o- and e-polarized photon pairs therefore carry a su-
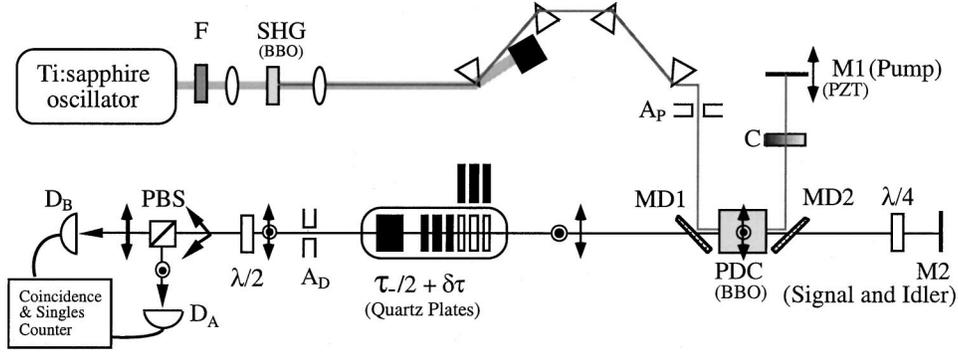
FIG. 2. Schematic of the pulse-pumped collinear Hong-Ou-Mandel interferometer with a spectrally symmetrized source. A pump pulse passes through the parametric downconverter (PDC) and is separated from the downconverted light by means of a dichroic mirror MD2. The pump pulse is reflected back into the PDC by mirror M1, and passes twice through a dispersion and intensity compensator plate (C). The signal and idler beams are reflected back via M2, with their polarizations exchanged by the λ/4 plate. The photon pairs that ultimately emerge from the downconverter could have been generated on either the first or second pass of the pump through the crystal. The downconversion from this modified source is separated from the outgoing pump beam by MD1 and sent through a delay line, polarization rotator, and polarizing beamsplitter before impinging onto a pair of photodetectors. Coincidence counts are collected and recorded electronically.

perposition of the joint emission amplitude spectra for each process, given by

$$f'(\omega_o,\omega_e)=f(\omega_o,\omega_e)+e^{i\theta}f(\omega_e,\omega_o), \qquad (7)$$

where $f(\omega_o,\omega_e)$ refers to the fields generated on the first pass, $f(\omega_e,\omega_o)$ to those generated on the second, and

$$\theta=k_s(\omega_s)l_{signal}+k_i(\omega_i)l_{idler}-k_p(\omega_p)l_{pump} \qquad (8)$$

is the phase difference between the first and second downconversion process. This phase difference can be varied by changing l_{pump}, the optical path length of the pump arm, or by changing l_{signal} and l_{idler}, the optical path lengths of the two polarizations in the signal and idler arm. The optical path lengths include propagation through the dispersive media such as the downconversion crystal; this is discussed in detail in Appendix B. For suitable values of $\theta(0,\pm 2\pi,\dots)$, the joint emission amplitude spectrum can be made symmetric in accordance with Eq. (6).

After emerging from the PDC, the downconverted photons are separated from the pump with another dichroic mirror and sent into a common-path HOM interferometer of the type first demonstrated by Shih and Sergienko [26]. This consists of an adjustable birefringent delay line ($\tau_-/2 + \delta\tau$), a λ/2 plate, a polarizing beamsplitter (PBS), and a pair of photodetectors (D_A, D_B). The fixed birefringent delay of $\tau_-/2$ compensates for the average temporal walkoff between the x- and y-polarized photons in the PDC [see Eq. (21)]; the additional birefringent material then imposes a variable delay $\delta\tau$ between the photons before they enter the PBS. The λ/2 plate rotates both the x and y polarizations by 45°: each photon may then be either reflected or transmitted at the PBS, with equal probability. A coincidence count at the detectors could have come from transmission of the x- and reflection of the y-polarized photons, or vice versa. These two coincidence processes interfere with each other when they cannot be distinguished by auxiliary measurements of frequency, polarization, or relative arrival time, so

that the coincidence counting rate is altered as $\delta\tau \rightarrow 0$. In traditional HOM interferometers, this interference is always destructive, but in this experiment it is possible to arrange for either constructive or destructive interference to occur by adjusting θ.

QUANTUM STATE OF THE LIGHT

The quantum state describing a photon pair created by a single pump pulse can be obtained from a two-stage evolution in the interaction picture that describes the first and second downconversion processes (see Appendix A). The state of the downconverted light emerging from the PDC is

$$|\psi\rangle \cong |vac\rangle - \eta\delta\omega\sum_{\omega_o}\sum_{\omega_e}\alpha(\omega_o+\omega_e)\Phi(\omega_o,\omega_e)[|\omega_o\rangle_x|\omega_e\rangle_y$$

$$+ e^{i\theta}|\omega_o\rangle_y|\omega_e\rangle_x]$$

$$= |vac\rangle - \eta|\psi^{(1)}\rangle, \qquad (9)$$

where the labels x and y denote the two orthogonally polarized output modes, and the e and o labels denote the signal and idler frequencies. $\delta\omega$ is the mode spacing and η describes the magnitude of the perturbation on the initial vacuum state as defined in Appendix A; we have omitted terms of order η^2 and higher. θ is the relative phase of the origins for the two downconversion processes as defined in Eq. (8); for the moment, we will treat θ as being frequency-independent over the bandwidth of the signal, idler, and pump photons. We are restricting our calculations to the ''nondepleted pump'' regime, in which we assume

$$|\eta|^2\langle\psi^{(1)}|\psi^{(1)}\rangle \ll 1. \qquad (10)$$

The spectrum of a single pump pulse is assumed to have a normalized Gaussian form with bandwidth σ, centered on the frequency $2\bar{\omega}$,

$$\alpha(\omega_o+\omega_e)=\frac{2}{\sigma\sqrt{\pi}}e^{-[(\omega_o+\omega_e-2\bar{\omega})/\sigma]^2}, \qquad (11)$$

while the phase-matching function follows from Eq. (A11) in Appendix A:

$$\Phi(\omega_o,\omega_e)=\text{sinc}\left([k_o(\omega_o)+k_e(\omega_e)-k_p(\omega_o+\omega_e)]\frac{L}{2}\right). \quad (12)$$

Here L is the length of the PDC.

PREDICTED COUNTING RATES

Our experiment measured both single-channel and coincidence counts as the quartz delay $\delta\tau$ and phase θ were varied; we begin by calculating the single-channel counting rate at detector D_A as a function of these two parameters. For a single pump pulse, the probability that detector D_A registers a photon within a time interval dt around the time t is $p_A(t)dt$, with the instantaneous probability density given by

$$p_A(t;\delta\tau,\theta)=\langle\psi|\hat{E}_A^{(-)}(t)\hat{E}_A^{(+)}(t)|\psi\rangle. \quad (13)$$

Here $|\hat{E}_A|^2$ is in photons per second, and we are assuming perfect detection efficiency for D_A.

We may rewrite the instantaneous field operator at the detector as a Fourier decomposition of the polarization components of the signal and idler modes projected onto D_A by the $\lambda/2$ plate and PBS:

$$\hat{E}_A^{(+)}(t;\delta\tau)=\left(\frac{\delta\omega}{2\pi}\right)^{1/2}\sum_\omega\frac{1}{\sqrt{2}}[\hat{a}_x(\omega)e^{i\omega\delta\tau}+\hat{a}_y(\omega)]e^{-i\omega t}. \quad (14)$$

The total photodetection probability accumulated over all times is

$$P_A(\delta\tau,\theta)=\int_{-\infty}^{\infty}dt\,p_A(t;\delta\tau,\theta). \quad (15)$$

After substitution of Eqs. (14) and (9) into Eq. (13), we carry out the integration in Eq. (15) in the limit $\delta\omega\to0$. We then multiply the resulting detection probability by the pulse repetition rate and detection efficiencies to obtain a counting rate:

$$R_A(\theta)=R_{A0}\left\{\frac{1}{2}+\left[\frac{\sqrt{\pi}}{Z}\right]\text{erf}\left(\frac{Z}{4}\right)\cos(\theta)\right\}, \quad (16)$$

where

$$R_{A0}=4\alpha_A\beta_A R_p|\eta|^2 B \quad (17)$$

is twice the mean counting rate at D_A. Here α_A is the quantum efficiency of D_A; β_A is the fraction of emitted light transmitted through the optics to D_A; R_p is the repetition rate of the pump pulses; B is given by

$$B\equiv\int_0^\infty\int_0^\infty d\omega_o\,d\omega_e|\alpha(\omega_o+\omega_e)|^2|\Phi(\omega_o,\omega_e)|^2=\frac{4\sqrt{2\pi}}{\sigma\tau_-} \quad (18)$$

and Z is defined as

$$Z\equiv\sigma(\tau_o+\tau_e)/\sqrt{2}. \quad (19)$$

In this last definition,

$$\tau_o=L\left(\left.\frac{\partial k_p}{\partial\omega}\right|_{2\bar{\omega}}-\left.\frac{\partial k_o}{\partial\omega}\right|_{\bar{\omega}}\right) \quad (20)$$

is the maximum difference between the group delays experienced by the pump pulse and the o wave packet (after traveling the entire length of the PDC), τ_e is the analogous quantity for the e wave packet, and

$$\tau_-\equiv\tau_e-\tau_o \quad (21)$$

is the maximum group delay between the o and e wave packets.

The counting rate at D_B is computed in exactly the same fashion, giving a result analogous to that in Eq. (16), with twice the mean rate defined similarly as

$$R_{B0}=4\alpha_B\beta_B R_p|\eta|^2 B. \quad (22)$$

According to Eq. (16), then, both of the single-channel detection rates will vary sinusoidally with θ. This phenomenon, that the spontaneous downconversion process can be interferometrically enhanced or frustrated, was first demonstrated by Herzog et al. [27] with cw-pumped type-I downconversion, and it is to be expected in our scheme as well. But in our case, the degree of interference is determined by the product of the pump bandwidth and the crystal length in Eq. (19); as either of these parameters is increased, the single-channel interference modulation decreases. This happens because the amplitudes that are being made to interfere—an e ray and an o ray from each downconversion process— become more distinguishable in the time-frequency domain as the crystal is lengthened or as the pump pulse is shortened. One may think of this either as temporal distinguishability, owing to different rates of walkoff of the signal and idler photons away from their ''parent'' pump photon within the crystal, or as spectral distinguishability, owing to the fact that as the pump bandwidth increases, the signal and idler bandwidths do not increase by the same amount [19].

We now compute the expected coincidence counting rate. For a single pump pulse, the probability that D_A registers a photon within a time interval dt_A centered at time t_A and that D_B registers a photon within dt_B centered at t_B is $p_{AB}(t_A,t_B)dt_A dt_B$. The instantaneous probability density p_{AB} is given by the normally ordered expectation value

$$p_{AB}(t_A,t_B;\delta\tau,\theta)=\langle\psi|:\hat{E}_A^{(-)}(t_A)\hat{E}_A^{(+)}(t_A)$$
$$\times\hat{E}_B^{(-)}(t_B)\hat{E}_B^{(+)}(t_B):|\psi\rangle. \quad (23)$$

We obtain the total probability for a coincidence count by integrating p_{AB} over all possible photon arrival times within the coincidence resolving time; because this time is already long compared to the coherence time of the light, the limits of these integrations can be extended to $\pm\infty$:
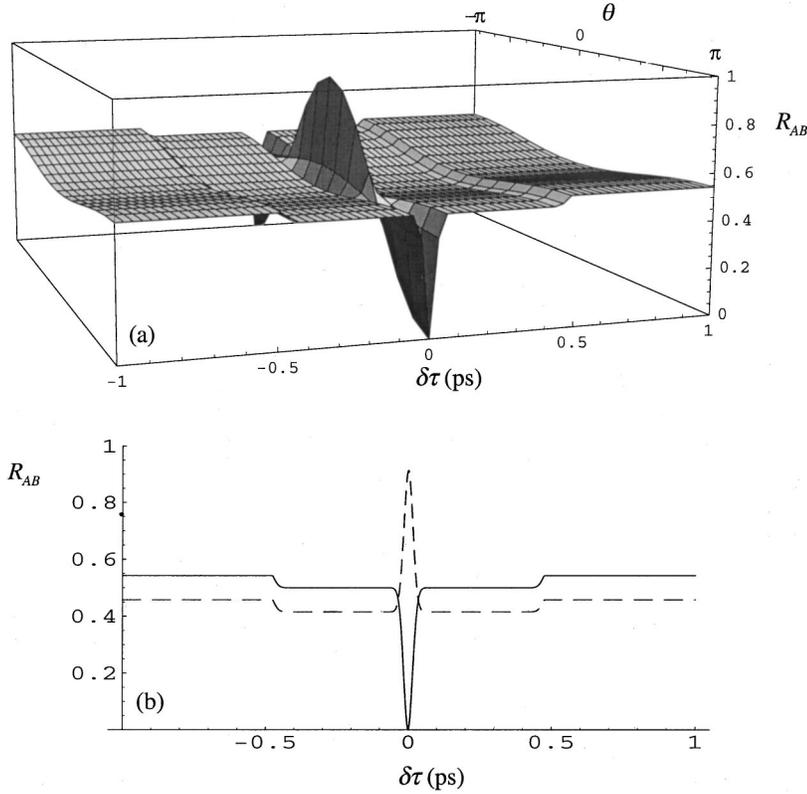
FIG. 3. (a) The coincidence counting rate $R_{AB}(\delta\tau,\theta)$ shows sinusoidal modulation as θ is varied, with a visibility that depends on the value of $\delta\tau$. For fixed values of θ, the variation with $\delta\tau$ is a modified version of the familiar type-II Hong-Ou-Mandel ''dip'' structure. In particular, the value $\theta=0$, which symmetrizes the joint amplitude emission spectrum for the photons, leads to coincidence counts that dip all the way to zero (b, solid line). The width of this dip is determined by the pump bandwidth and the PDC crystal length. For $\theta=\pi$, the spectrum is antisymmetric and results in an interference peak instead of a dip (b, dashed line); the peak does not reach unity because of a residual destructive HOM interference effect in the trough region of width $-0.5\,\text{ps}<\delta\tau<0.5\,\text{ps}$ (determined only by the PDC crystal length). Plots were made for $R_{AB0}=1$ using the parameters $\sigma=34.5\,\text{ps}^{-1}$, $\tau_o=0.38\,\text{ps}$, and $\tau_e=1.33\,\text{ps}$ corresponding to the 5-mm-long BBO downconverter in our experiment.

$$P_{AB}(\delta\tau,\theta) = \int_{-\infty}^{\infty}\int_{-\infty}^{\infty} dt_A dt_B \, p_{AB}(t_A,t_B;\delta\tau,\theta). \quad (24)$$

After performing these integrations in a fashion analogous to the above, we obtain[2]

$$
\begin{aligned}
R_{AB}(\delta\tau,\theta) = R_{AB0}&\left(\frac{1}{2} + \cos(\theta)\frac{\sqrt{\pi}}{Z}\text{erf}\left(\frac{Z}{4}\right) \right.\\
&- \left\{ \cos(\theta)\left(\frac{1}{2}-\frac{|\delta\tau|}{\tau_-}\right)e^{-[Z\delta\tau/\tau_-]^2} \right. \\
&\left. + \frac{\sqrt{\pi}}{Z}\text{erf}\left[\frac{Z}{2}\left(\frac{1}{2}-\frac{|\delta\tau|}{\tau_-}\right)\right] \right\} \\
&\left. \times \text{rect}\left(\delta\tau; \frac{-\tau_-}{2}, \frac{\tau_-}{2} \right) \right),
\end{aligned}
\quad (25)
$$

where

$$R_{AB0} = 2\alpha_A\alpha_B\beta_A\beta_B R_p |\eta|^2 B \quad (26)$$

is twice the mean coincidence counting rate for $|\delta\tau| > \tau_-/2$, averaged over θ—this is the average rate at which our source produces photon pairs, multiplied by the collection and detection efficiencies. This corresponds to twice the observed ''baseline'' rate because, even in the absence of

---

[2]The following equation corresponds to Eq. (8) in Ref. [23], which contains a typographical error.

HOM and Michelson interference, only two of the four possible outcomes at the beamsplitter can generate coincidence counts.

A plot of $R_{AB}(\delta\tau,\theta)$ is shown in Fig. 3(a), with $R_{AB0}=1$. For the fixed value $\theta=0$, which symmetrizes the state in Eq. (9), we expect to see the modified HOM dip structure shown in Fig. 3(b) (solid line). The coincidence rate falls to zero as $\delta\tau\to 0$, indicating full recovery of the quantum interference of the photon pairs. For the value $\theta=\pi$, we expect to observe a ''peak'' structure as $\delta\tau\to 0$ [Fig. 3(b), dashed line]. As θ is varied while $\delta\tau$ is kept fixed, sinusoidal interference fringes between the peak and dip values are expected. For $\delta\tau=0$, these fringes should have 100% visibility, and should be 180° out of phase with the single-channel fringes predicted by Eq. (16). These fringes are generated by the third term in Eq. (25). As $\delta\tau$ is shifted away from zero, the magnitude of this term rapidly diminishes due to its narrow Gaussian character, and the visibility of the fringes is reduced; they remain out of phase with the single-channel fringes until the crossing point where $\delta\tau$ satisfies

$$\left(\frac{1}{2}-\frac{|\delta\tau|}{\tau_-}\right)e^{-[(Z/\tau_-)\delta\tau]^2} = \frac{\sqrt{\pi}}{Z}\text{erf}\left(\frac{Z}{4}\right). \quad (27)$$

At this point, the third term in Eq. (25) has diminished to the same magnitude as the second term, which has a small value independent of $\delta\tau$ and gives rise to fringes that are in phase with the single-channel counts. At the crossing point, these two terms cancel each other and there are no fringes whatsoever. For larger $\delta\tau$ values up to $|\delta\tau| = \tau_-/2$, the second term dominates to produce low-visibility fringes in phase with the single-channel counts; this region of $\delta\tau$ corresponds

to the previously identified HOM interference ''trough'' [22]—a truncated version of the usual type-II HOM dip that does not exhibit complete destructive interference because of chronocyclic distinguishing information. But here the entire trough, and even the baseline rate for $|\delta\tau| > \tau_-/2$, exhibits modulation as θ is varied; this coincidence modulation is an artifact of the single-channel oscillations governed by Eq. (16).

The HOM trough is the normal result of two-photon interference with a pulse-pumped type-II PDC. Figure 3 shows that over a small region of this trough, the dip visibility can be completely restored. But our symmetrized source does not have the effect of restoring the complete triangular-shaped dip common to cw-pumped type-II HOM interference [26]. The width of the central Gaussian dip (and peak) is governed by the parameter Z defined in Eq. (19); as the crystal length or pump bandwidth increases, the width of this high-visibility dip decreases. When $\delta\tau$ exceeds the amount of delay at the crossing point (27), only the normal HOM interference for an unsymmetrized source is taking place—albeit, with a baseline rate that is modulated by the single-channel interference in Eq. (16). Evidently, there is only a small range of polarization delays $\delta\tau$ over which it is impossible to determine not only which photon (e or o) ends up at which detector, but also whether the photon pair originated in the first or second pass of the pump pulse. Longer crystal lengths imply larger amounts of temporal walkoff for the photons from each other and from their ''parent'' pump photon, making it easier to identify from which process a given pair must have originated in order to be consistent with their observed relative arrival times: shorter pump pulses make this sort of timing distinction more precise (see Fig. 12 and the discussion at the end of Appendix B).

EXPERIMENTAL DETAILS

The Ti:sapphire oscillator was tuned to operate at 810 nm. This light was doubled to 405 nm with a 0.7-mm-long β-barium-borate (BBO) crystal cut and aligned for type-I phase matching. This delivered an average pump power of 330 mW, with a pulse repetition rate of 80 MHz. The measured bandwidth of the pump was $\Delta\lambda_p \approx 3$ nm, implying $\sigma = 34.5$ ps^{-1} and a coherence length $L_p \approx 50\ \mu$m.

The downconversion crystal was a 5-mm-long piece of BBO, cut for collinear type-II phase matching at 405 nm so that its optic axis was at an angle of 41.8° to the normal of the input face. The crystal was aligned by maximizing the production of upconverted light when the 810-nm oscillator was sent backwards through the quartz delay and interferometer. The $\lambda/4$ plate was a zero-order quartz waveplate, approximately 1.5 mm thick.

We attempted to balance the losses and dispersion for the signal and idler arm (see Appendix B) by placing a compensator plate (C) in the pump arm. This was a BK-7 glass slide with a neutral-density gradient along its length. The slide was mounted on a translation stage, so that more or less transmissive parts of the slide could be inserted into the pump beam until the intensities coming from the two arms were equalized. The 1.58-mm thickness also served to cancel

most of the second-order dispersion experienced by the signal and idler photons.

The mirror M1 was mounted on a piezoelectric transducer (PZT) and a motorized translation stage. The phase difference θ was varied by changing L_p with the PZT. An active locking system ensured the stability of the Michelson interferometer by sending negative feedback to the PZT, so that θ could be held constant while the photons were counted. The error signal for this negative feedback was derived from changes in the position of a set of interference fringes that were generated by injecting a HeNe laser beam into the Michelson interferometer. This locking system was able to keep L_p constant to within $\Delta L \approx 20$ nm; from Eq. (B4) in Appendix B, this implies a stability in θ of $\Delta\theta^{(0)} \approx 2\pi/20$.

The delay line for varying $\delta\tau$ consisted of a set of six crystal quartz plates, four of thickness 1 mm and two of thickness 0.5 mm. The plates remained in the beam at all times, and were oriented with their fast axes aligned either to the e or o polarization of the BBO crystal. Different combinations of orientations for the plates resulted in different net delays between the signal and idler photons. A fixed delay compensator plate was also inserted to cancel the average temporal walkoff in the BBO crystal, $\tau_-/2$, so that the photon pairs would experience only the net delay specified by $\delta\tau$. For a 5-mm piece of BBO, the appropriate delay compensator was a 16.2-mm quartz plate with its fast axis oriented to the o axis of the BBO.

The photodetectors (D_A and D_B) were avalanche photodiodes (APD's) that generated electronic pulses whenever a photon was registered. These pulses were inverted and sent to discriminators that generated uniform pulses triggered on the leading edge of each APD pulse. These pulses were then fed to a coincidence counter that produced an output pulse whenever the two inputs arrived within 200 ns of each other.

After aligning the system, we typically achieved coincidence count rates of around 4000/s with all apertures wide open. To compensate for poor mode matching of the two downconversion processes at the crystal, we closed aperture A_P to 2-mm and A_D to 1-mm diam, which improved the interference. The mean single channel rates were then around 3000/sec, while the mean coincidence rate was roughly 15/s. From these numbers and the relations (17), (22), and (26), we find

$$\alpha_A\beta_A = \alpha_B\beta_B \cong 0.01 \qquad (28)$$

and, with $R_p = 8\times10^7$,

$$|\eta|^2 B \approx 10^{-3}, \qquad (29)$$

which ensures that the nondepleted pump approximation (10) is well satisfied.

EXPERIMENTAL RESULTS

We collected photocounts for 11 different values of $\delta\tau$, covering the range $-0.16 < \delta\tau < 0.16$ ps. For each value of $\delta\tau$, we recorded counts at 11 different θ values, producing

interference fringes in both the single-channel and coincidence counts. The pump mirror was displaced while the interferometer remained actively stabilized, by translation of the photodiodes that used the position of a separate fringe pattern generated by a HeNe laser to generate an error signal. A translation of these diodes through $1450 \pm 50 \, \mu m$ corresponded to 2π radians of displacement in θ, as determined from sinusoidal fits to the single-channel fringes we obtained. Counts were collected for 200 s at each θ value. The total time for all scans was 9 h. During that time, the laser power dropped steadily from its initial value, and realignment was forbidden once the data collection began. Therefore, the average pump power was measured during the course of each data-taking interval, so the drop in power could be divided out. The data presented and analyzed here have all been renormalized in this way.

Data for three particular values of $\delta\tau$ are shown in Fig. 4. The lines represent the best fits of the data to sinusoidal curves. As predicted, the low-visibility[3] (6%) coincidence fringes for large $\delta\tau$ are in phase with the low-visibility (3%) single-channel fringes, while the high-visibility (64%) coincidence fringe near the center is out of phase with the single-channel fringes recorded there. This is in stark contrast to earlier experiments that involved the coherent superposition of two downconversion processes [27–29] but did not use pulsed pumping or HOM interference. In those experiments, the modulation of the coincidence rate was a direct consequence of the modulation in the pair-creation rate, so that the coincidence and single-channel counts were always in phase with each other as θ was varied. In our case, the coincidence modulation occurs in spite of, and not because of, the single-channel modulation; it also has a higher visibility because the coincidence detection paths are much less spectrally distinguishable than either single-channel detection path alone.

All of the coincidence data are plotted in Fig. 5(a) as a function of $\delta\tau$ and θ. The data with positive $\delta\tau$ values were renormalized to account for a systematic error related to the orientation of a particular quartz plate. The resulting picture should be compared to the theoretical plot in Fig. 5(b), which includes the effects of dispersion and path-length imbalance in the experiment (see Appendix B).

A maximum fringe visibility of 64% was observed for the scan at $\delta\tau=0$. There are several reasons why this visibility did not reach 100%. To begin with, the losses in the Michelson interferometer were not equal for the two arms, despite our efforts to balance them with the compensator plate (C). Scans taken with each arm of the interferometer blocked revealed that the signal and idler arm contributed a mean intensity of 959 ± 52 counts/200 s, while the pump arm contributed 1348 ± 30 counts/200 s (these values were obtained from repeated measurements of each contribution, and the uncertainties correspond to the standard deviation of these measurements). Even so, the maximum possible interference vis-

---

[3]Unless otherwise noted in this paper, we use the term "visibility" in the way that is customary for sinusoidal interference patterns: the difference of the maximum and minimum count rates, divided by their sum.
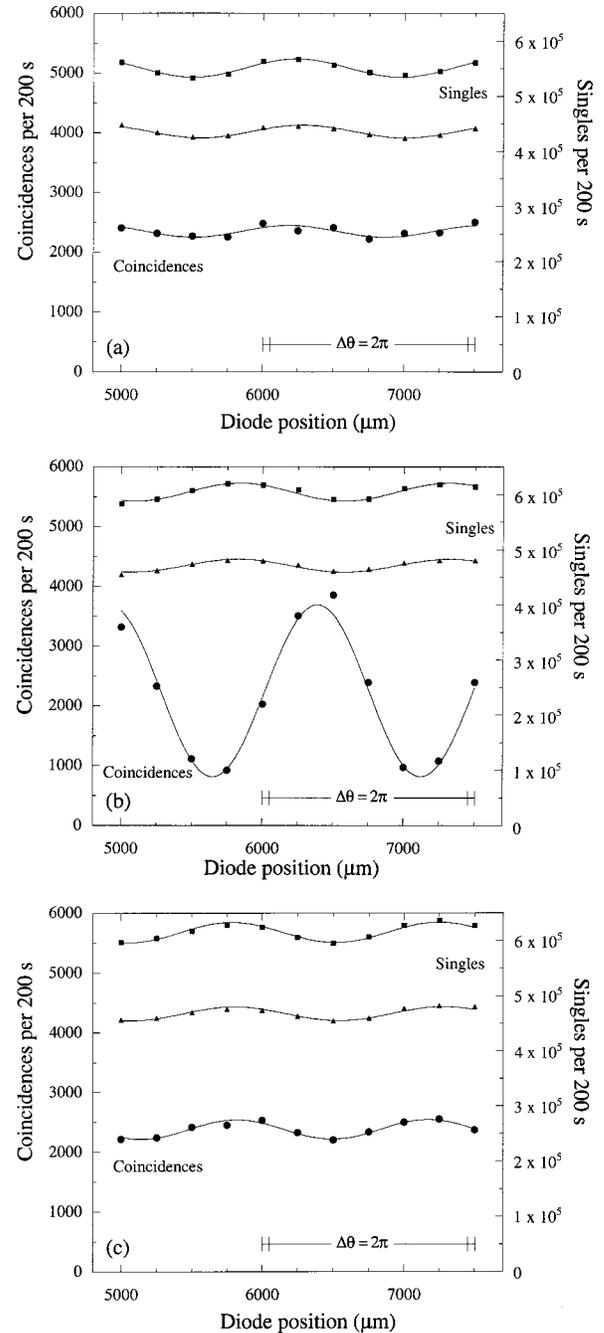

FIG. 4. Recorded coincidence and single-channel counts as a function of the pump mirror displacement, for fixed values of the delay $\delta\tau=-0.16$ ps (a), $\delta\tau=0$ ps (b), and $\delta\tau=+0.16$ ps (c). The pump mirror was displaced by translating a pair of locking photodiodes that provided feedback to the PZT; this produced variations in θ of the scale indicated in the lower right corner of each plot. The counts have been renormalized to eliminate the effects of laser power drifts. The interference visibility reached 64% for the case $\delta\tau=0$. Note that the coincidence fringe is almost completely out of phase with the single-channel fringes at $\delta\tau=0$, while the fringes for $\delta\tau=\pm16$ ps are all in phase with one another. That the coincidence and singles fringes at $\delta\tau=0$ are not perfectly out of phase is due to a -10-μm error in the position of M1, which implies that the true point of maximum HOM interference requires a slightly different quartz delay (see Appendix B).
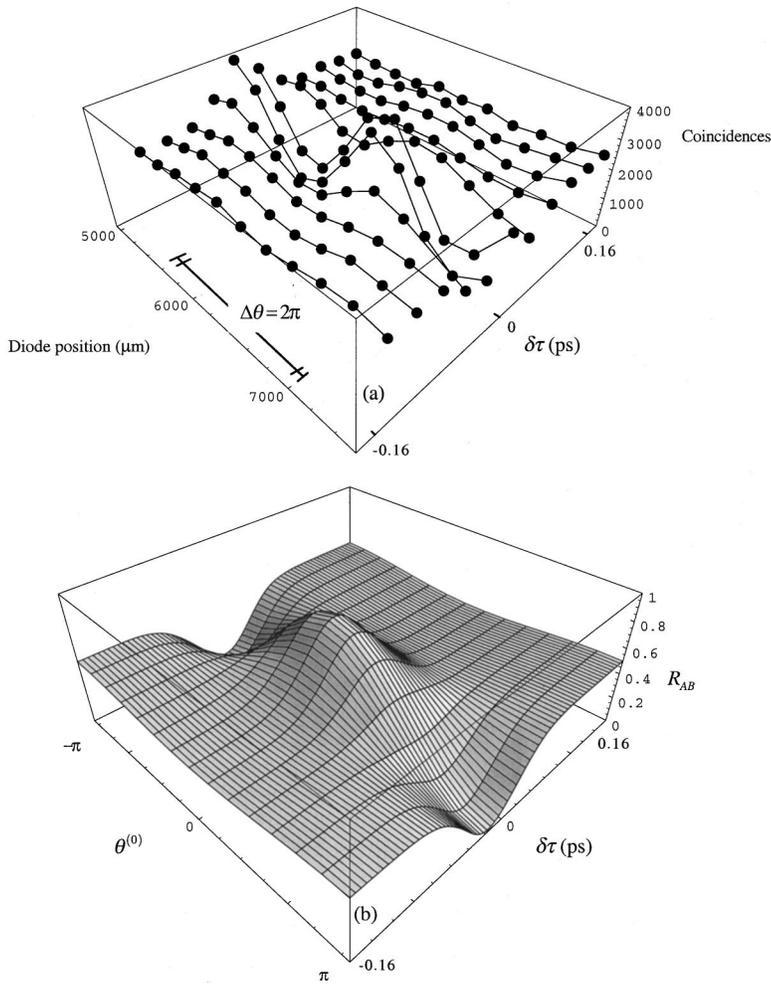
FIG. 5. (a) Compilation of all eleven renormalized coincidence fringes, recorded over the range $-0.16 < \delta\tau < 0.16$ ps. Note the change in the position of the maximum of each fringe with respect to the diode position (θ); the fringes appear to ''drift'' in their phase as more quartz delay is added. The theoretical prediction in (b) does not indicate this drift. (The theory includes a -10-μm shift in the position of M1.)

ibility allowed under these conditions is $2\varepsilon/(1+\varepsilon)^2 = 0.98$, where ε^2 is the ratio of the two mean intensities. Further degradation of the interference can be caused by dispersion in the interferometer, but calculations show that this effect should be slight for our particular experiment (see Appendix B). We believe that the main difficulty in achieving high visibility arises from the distinguishability of the spatial modes associated with downconversion from the first and second passes through the crystal. Because the two sources contributing to the final events are actually at different optical distances from the PBS, it is difficult to properly image both for complete interference. This problem has been analyzed for another two-source downconversion experiment [30].

Because the success of our symmetrization technique for creating entanglement can be judged by improvement in the HOM interference null, we will now look at the other cross section of the data set in Fig. 5: that is, we will examine the structure of the coincidence dip as $\delta\tau$ is varied, for fixed values of θ. The maxima and minima implied by the sinusoidal fits for all 11 values of $\delta\tau$ are plotted in Fig. 6. The solid line is a plot of the counting rate predicted by Eq. (B11) that includes the appropriate amounts of dispersion, a 10-μm error in the position of M1, and the unequal losses in the Michelson interferometer (see Appendix B). The calculation was scaled by setting the mean of all the maxima and
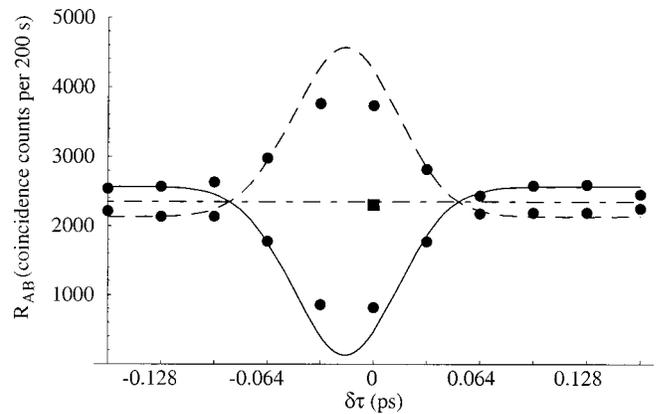

FIG. 6. Minimum and maximum coincidence counting rates (per 200 s) extracted from experimental data for 11 values of $\delta\tau$, corresponding to the central region of Fig. 3(b) (all points here are well inside the trough region of that figure). The square is the incoherent sum of the rates for the two processes. The dot sizes correspond to one standard deviation of statistical uncertainty. Also shown are theoretical curves for $\theta = 0$ (solid), $\theta = \pi$ (dashed), and for the unsymmeterized source (dot-dashed line). In these plots, as in Fig. 3, the width of the central interference dip is determined by the pump bandwidth and the crystal length.

minima, 2347 ± 39 counts/200 s, equal to the θ-averaged counting rate inside the trough as predicted by Eq. (B11); the result is $R_{AB0} = (2347 \pm 39)/(0.5 - 0.0428) = 5134 \pm 85$ counts/200 s. Though our observed visibilities do not reach the maximum allowed by the theory, it is still apparent that the HOM interference has been improved by our technique, because the minimum counting rate is significantly lower with the symmetrized source (circles) than that of an unsymmetrized source (square).

Unfortunately, we did not have quartz plates with appropriate lengths to directly measure the baseline coincidence counting rate outside the trough. We attempted to achieve the required delays of $\delta\tau > 0.5$ ps by using several additional thin plates, but the counting rates and visibilities were then reduced to intolerable levels by the cumulative losses and polarization errors introduced by each plate. This means that we do not have direct measurements of the dip visibility[4] for the symmetrized and unsymmetrized cases. However, we know that the baseline counting rate should be half the value of R_{AB0}, or 2567 ± 43 counts/200 s; the lowermost data point on the plot in Fig. 6 corresponds to a minimum counting rate of 817 ± 53 counts/200 s, which gives a dip visibility of $(68 \pm 3)\%$ for our symmetrized source. In contrast, the observed counting rate for the unsymmetrized source is 2306 ± 53, which corresponds to a dip visibility of only $(10 \pm 4)\%$.

DISCUSSION

The minimum and maximum count values plotted in Fig. 6 represent the conditions $\theta = 0$ and $\theta = \pi$, respectively, for values of $\delta\tau$ that lie between the crossing points satisfying Eq. (27). Outside this range, the situation is reversed, with the minimum count values corresponding to $\theta = \pi$ and the maxima corresponding to $\theta = 0$. The theory predicts a sharp transition between these two regions (solid line, Fig. 7), marked by an interference visibility of zero at the crossing point (where the solid and dashed lines meet in Fig. 6). However, this sharp transition in the relative phases was not observed. Instead, our coincidence data displayed a smooth phase drift as $\delta\tau$ increased [see Fig. 5(a)] while the phase of the single-channel fringes remained constant.

The relative phase of the coincidence and single channel sinusoidal fits is plotted in Fig. 7; the relative phase appears to vary linearly with $\delta\tau$, as shown by the dots. This phase drift is not predicted by our theory. A close inspection of Eq. (B11) does reveal that, in principle, the fringe attributed to the third term of the counting rate will have an additional phase that depends on $\delta\tau$. However, calculations showed that this phase shift is not appreciable even with 10 times the amount of dispersion present in our interferometer. Furthermore, the magnitude of this term, which is generating the enhanced dip structure, falls to zero fairly quickly as $|\delta\tau|$ increases, whereas the observed phase shift persists over the entire region of our data.

----

[4]The term ''dip visibility'' applies only to HOM interference patterns, and is here defined to be the difference of the minimum and baseline coincidence counting rates, divided by the baseline rate.
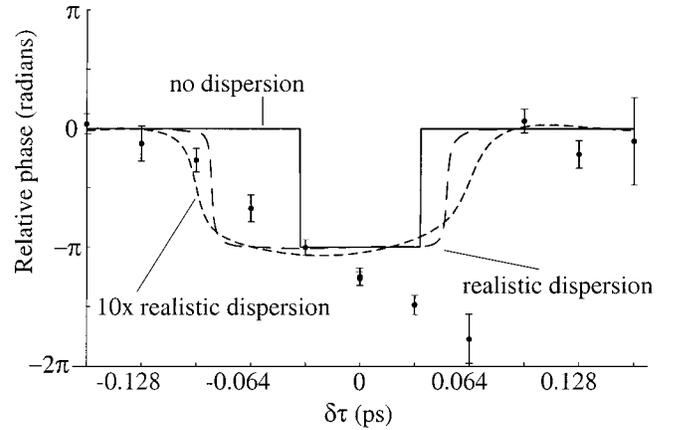

FIG. 7. The phase of the coincidence fringes relative to the single-channel fringes does not undergo a sharp transition as predicted by the dispersionless theory (solid line), but instead varies smoothly with $\delta\tau$ over the range of our data. The uncertainty in each observed relative phase was estimated by propagation of the uncertainties in the phases of the sinusoidal fits to the corresponding single-channel and coincidence fringes. When realistic amounts of dispersion are included (long-dashed line), the theory predicts a smoother transition, but still does not reproduce the observed linear phase drift. With ten times the actual amount of dispersion (short-dashed line), the transition is smoother but still does not agree with our observations. The dashed line curves also include the effects of a -10-μm shift in L_p, the pump mirror position. The two data points at $\delta\tau = 0$, taken with different combinations of quartz plates, differ by 0.008 radians and have uncertainties of 0.22 and 0.19 radians.

It appears unlikely that this trend is the result of a systematic error. The interferometer remained locked at all times in each of these regions, and the single channel fringes reflect this in that their phases did not drift from scan to scan; therefore, the systematic error would have to produce a drift only in the phase of the coincidence counts. Additionally, the phase drift never changed direction with regard to $\delta\tau$, despite the fact that the time order of the scans for $\delta\tau \lesssim 0$ was opposite that of the scans for $\delta\tau > 0$; therefore, it seems more likely that any systematic effects would be tied to the quartz plates themselves. But since different sets of plates were changed each time to produce the various delays, one would expect a quartz-related effect to produce essentially random phase changes with respect to $\delta\tau$. Instead, the phase drift appears insensitive to how specific plates were oriented, and instead depends only on the total amount of quartz involved. Indeed, when a second scan was taken at $\delta\tau = 0$ with a different combination of quartz plate orientations, the relative phase was nearly identical to that of the first scan (see Fig. 7).

We can only conclude that the phase drift between the coincidence and single-channel fringes is a genuine effect, sensitive to $\delta\tau$, that is unaccounted for by the present theory. A recent paper by Atatüre *et al.* [31] has called attention to another HOM interference effect in ultrafast-pumped type-II PDC that seemingly cannot be accounted for using the standard quantum description—namely, an asymmetry in the dip structure that grows more pronounced with PDC length.

Their solution is to add a ''partial decoherence function'' by hand into the evolution of the state, which represents the irreversible introduction of distinguishing information as the photon pairs propagate away from the pump pulse in the dispersive PDC medium. This approach certainly offers another perspective that might explain our observed phase drift, but our hopes are diminished for two reasons. First, the effects of dispersion in the PDC are already accounted for in the present theory. Second, our central dip structure is in fact symmetric, so that any decoherence that occurred during the first pass through the PDC would have to be *undone* during the second pass. This appears problematic, since the pairs created in the first process encounter a larger amount of dispersive material than those created in the second; it also appears inconsistent with the irreversible nature of the ''partial decoherence function.''

In conclusion, we have demonstrated the operation of a source of frequency-entangled photon pairs that works by suppressing distinguishing information in the time-frequency domain. Our experiment shows that a high degree of interference can be achieved even with a long type-II PDC crystal without postselection of the events with spectral filters, and while retaining the synchronization benefits available with ultrafast pumping. The method is general enough to allow the entanglement of both the space-time and polarization components of the state vector, and is especially useful for situations where the single-pass state is not highly entangled, as is often the case in parametric downconversion.

APPENDIX A: QUANTUM STATE DERIVATION

Initially, we consider the downconversion produced by a single pump pulse on its first pass through the crystal. The interaction Hamiltonian is

$$H_I = \tfrac{1}{2} \int_V d^3r \, \hat{\mathbf{E}}(\mathbf{r},t) \cdot \chi^{(2)} \hat{\mathbf{E}}(\mathbf{r},t) \hat{\mathbf{E}}(\mathbf{r},t), \qquad (A1)$$

where $\chi^{(2)}$ is the second-order electric susceptibility tensor for the medium.

The pump pulse is considered to be an intense coherent field that it is not significantly affected by the occasional annihilation of one photon. We therefore treat it classically, with an electric field given by

$$\mathbf{E}_p^{(+)}(t) = V_0 \upsilon(z-ct)\varepsilon_e e^{i[\mathbf{k}_p(\omega_p)\cdot\mathbf{r} - \omega_p t]}. \qquad (A2)$$

Here V_0 represents the maximum amplitude of the pump field, while $\upsilon(z-ct)$ is a dimensionless ''envelope'' function that propagates in the z direction. The envelope function may be complex, to reflect a ''chirped'' or other complicated
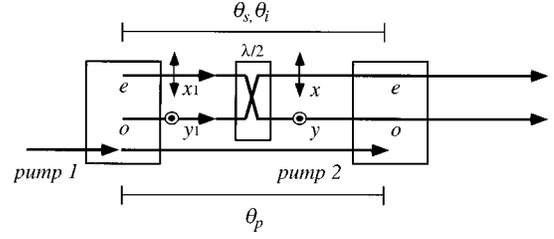

FIG. 8. Input and output modes for the two-stage interaction that creates a pair of signal and idler photons.

phase structure. The pump beam is assumed to have a linear polarization ε_e along the extraordinary axis of the crystal, while the signal and idler fields are assumed to have polarizations along the ordinary (o or y) and extraordinary (e or x) axes, respectively, as demanded by the type-II phase-matching considerations.

The downconverted fields are represented by Fourier sums of discrete-frequency field operators with orthogonal polarizations; the frequencies are ω_e, ω_o and the polarizations are $x1, y1$ (see Fig. 8). After inserting the sum of the pump, signal, and idler fields into Eq. (A1) and retaining only those terms that give nonzero contributions for the initial vacuum state, we have

$$\hat{H}_{I1} = \frac{1}{2}\frac{\delta\omega}{2\pi}\sum_{\omega_o}\sum_{\omega_e} V_0 \tilde{\chi}^{(2)}_{eoe}\varepsilon_e\varepsilon_o^*\varepsilon_e^* l_x l_y$$

$$\times \int_z dz\, e^{-i(\omega_p+\omega_o-\omega_e)t}e^{i(k_p+k_o-k_e)z}\upsilon(z-ct)$$

$$\times a_{y1}^\dagger(\omega_o)a_{x1}^\dagger(\omega_e) + \text{H.c.} \qquad (A3)$$

for the interaction Hamiltonian governing the first pass of the pump pulse through the medium. The quantity $\delta\omega = 2\pi c/L_Q$ is the mode spacing within a one-dimensional ''quantization length'' of dimension L_Q, and $k \equiv \omega/c$. The $l_{x,y}$ are the transverse dimensions of the interaction region.

The state after the initial pass of the pump pulse through the PDC is calculated via the usual Taylor series approximation to the Schrödinger evolution over the interaction time T, giving

$$|\psi_1(T)\rangle \cong \Bigg[1 + \frac{gV_0 l_x l_y}{i\hbar}\int_0^T dt' \frac{\delta\omega}{2\pi}\sum_{\omega_o}\sum_{\omega_e}$$

$$\times \int_z dz\, e^{-i(\omega_p-\omega_o-\omega_e)t}e^{i(k_p-k_o-k_e)z}\upsilon(z-ct')$$

$$\times \hat{a}_{y1}^\dagger(\omega_o)\hat{a}_{x1}^\dagger(\omega_e) + \text{H.c.}\Bigg]|\text{vac}\rangle, \qquad (A4)$$

where $g \equiv \tilde{\chi}^{(2)}_{eoe}\varepsilon_e\varepsilon_o^*\varepsilon_e^*$ and we have dropped terms of order g^2 and higher that contain four or more photons. Next we let

$$ct'' = z - ct' \qquad (A5)$$

so that

$$|\psi_1(T)\rangle = \left[1 + \frac{g V_0 l_x l_y}{i\hbar} \frac{\delta\omega}{2\pi} \sum_{\omega_o} \sum_{\omega_e} \right.$$

$$\times \int_z dz \, e^{i\{[k_p(\omega_p) - k_o(\omega_o) - k_e(\omega_e)] - (\omega_p - \omega_o - \omega_e)/c\}z}$$

$$\times \int_{z/c-T}^{z/c} dt'' w(ct'') e^{i(\omega_o + \omega_e)t''} \hat{a}_{y1}^\dagger(\omega_o) \hat{a}_{x1}^\dagger(\omega_e)$$

$$\left. + \text{H.c.} \right] |\text{vac}\rangle \tag{A6}$$

with the full time dependence of the pump field represented by the complex amplitude

$$w(t) \equiv \nu(ct) e^{i\omega_p t}. \tag{A7}$$

Because $w(t'')$ is nonzero only for a small range of times, the limits of the time integral may be extended to $\pm\infty$, so that the state is then given by

$$|\psi_1\rangle = \left[1 + \eta \delta\omega \sum_{\omega_o} \sum_{\omega_e} \alpha(\omega_o + \omega_e)\Phi(\omega_o, \omega_e) \right.$$

$$\left. \times \hat{a}_{y1}^\dagger(\omega_o)\hat{a}_{x1}^\dagger(\omega_e) + \text{H.c.} \right] |\text{vac}\rangle, \tag{A8}$$

where

$$\eta \equiv \frac{g l_x l_y l_z V_0}{i\hbar} \tag{A9}$$

is a dimensionless creation efficiency parameter,

$$\alpha(\omega) \equiv \frac{1}{2\pi} \int_{-\infty}^{\infty} dt \, w(t) e^{i\omega t} \tag{A10}$$

is the Fourier transform of the temporal profile of the pump pulse, and

$$\Phi(\omega_o, \omega_e) = e^{i[k_p(\omega_o + \omega_e) - k_s(\omega_o) - k_i(\omega_e)]z_o} \text{sinc}\{\tfrac{1}{2}[k_p(\omega_o + \omega_e)$$

$$- k_s(\omega_o) - k_i(\omega_e)]L\} \tag{A11}$$

is the phase-matching function produced by the z integral in Eq. (A6) for a downconversion crystal of length L, centered at position z_0. We will choose the origin for the z dependence of the field operators to be at the center of the crystal, so that $z_0 = 0$. We have dropped the dependence on T in the notation for $|\psi_1\rangle$, with the understanding that the state is valid (up to a phase) for all times after the first interaction is completed and before the second one begins.

After passing through the $\lambda/4$ plate twice and being reflected back into the downconversion crystal, the signal and idler photons have their polarizations exchanged, while their frequencies are preserved. As shown in Fig. 8, the field operators for the modes returning to the crystal are therefore related to the ''process one'' signal and idler modes by

$$\hat{a}_x(\omega_o) = -\hat{a}_{y1}(\omega_o),$$

$$\hat{a}_y(\omega_e) = \hat{a}_{x1}(\omega_e). \tag{A12}$$

Thus, the state before the second pass of the pump pulse may be rewritten in terms of the final field modes as

$$|\psi_1\rangle = |\text{vac}\rangle - \eta \delta\omega \sum_{\omega_o} \sum_{\omega_e}$$

$$\times \alpha(\omega_o + \omega_e)\Phi(\omega_o, \omega_e)|\omega_o\rangle_x |\omega_e\rangle_y, \tag{A13}$$

where we have introduced the notation $|\omega_{o,e}\rangle_{x,y} \equiv \hat{a}_{x,y}^\dagger(\omega_{o,e})|\text{vac}\rangle$ for a Fock state with a single photon in the signal or idler modes.

The origins of the signal and idler modes for the second downconversion process, which are again taken to be at the center of the PDC, have phases $\theta_s = k_s(\omega_s)l_{\text{signal}}$ and $\theta_i = k_i(\omega_i)l_{\text{idler}}$ relative to those of the first process; meanwhile, the pump pulse has acquired a phase $\theta_p = k_p(\omega_p)l_{\text{pump}}$ during its propagation to M1 and back. Here l_{signal}, l_{idler}, and l_{pump} are the optical path lengths of the signal, idler, and pump beams, as measured from the center of the PDC to the mirrors and back.[5] The interaction Hamiltonian for the second downconversion process is therefore given by

$$\hat{H}_{I2} = \frac{1}{2} \frac{\delta\omega}{2\pi} \sum_{\omega_o} \sum_{\omega_e} e^{i(\theta_s + \theta_i - \theta_p)} g V_0 l_x l_y$$

$$\times \int_z dz \, e^{-i(\omega_p + \omega_o - \omega_e)t} e^{i(k_p + k_o - k_e)z} \nu(z - ct)$$

$$\times a_y^\dagger(\omega_o) a_x^\dagger(\omega_e) + \text{H.c.} \tag{A14}$$

Treating $|\psi_1\rangle$ as the initial state for the second process, the state of the light after the second interaction is

$$|\psi\rangle = \left[1 + \eta \delta\omega \sum_{\omega_o} \sum_{\omega_e} e^{i(\theta_s + \theta_i - \theta_p)} \alpha(\omega_o + \omega_e)\Phi(\omega_o, \omega_e) \right.$$

$$\left. \times \hat{a}_y^\dagger(\omega_o)\hat{a}_x^\dagger(\omega_e) + \text{H.c.} \right] |\psi_1\rangle. \tag{A15}$$

Letting the creation and annihilation operators act on $|\psi_1\rangle$ and keeping only the terms of lowest order in η gives

$$|\psi\rangle \cong |\text{vac}\rangle - \eta \delta\omega \sum_{\omega_o} \sum_{\omega_e} \alpha(\omega_o + \omega_e)\Phi(\omega_o, \omega_e)$$

$$\times [|\omega_o\rangle_x |\omega_e\rangle_y - e^{i(\theta_s + \theta_i - \theta_p)}|\omega_o\rangle_y |\omega_e\rangle_x]. \tag{A16}$$

The minus sign in the brackets shows that our apparatus is not adding the two processes together, as mandated by Eq.

---

[5]This does not imply that all of the photons are emitted from the center of the PDC. The phases $\theta_{s,i,p}$ link the origins for the field mode operators from the first and second downconversion processes: these operators are then explicitly integrated over the PDC length for each interaction.

(3), but is instead subtracting them. For consistency, we therefore define $\theta \equiv \theta_s + \theta_i - \theta_p + \pi$, so that $\theta = 0$ corresponds to the symmetrized, and not the antisymmetrized, state:

$$|\psi\rangle \cong |\text{vac}\rangle - \eta\delta\omega \sum_{\omega_o} \sum_{\omega_e} \alpha(\omega_o + \omega_e)\Phi(\omega_o, \omega_e)$$

$$\times [|\omega_o\rangle_x |\omega_e\rangle_y + e^{i\theta}|\omega_o\rangle_y |\omega_e\rangle_x]. \quad \text{(A17)}$$

APPENDIX B: DISPERSION IN THE MICHELSON INTERFEROMETER

Underlying the calculation (9)–(25) is the assumption that θ, the relative phase between the origins for process 1 and process 2, is a frequency-independent quantity. However, this assumption is not strictly correct, as we can see by expanding Eq. (8) in a Taylor series about the mean signal, idler, and pump frequencies:

$$\theta(\omega_s, \omega_i) = [k_s(\bar{\omega})l_s + k_i(\bar{\omega})l_i - k_p(2\bar{\omega})l_p] + [(\omega_s - \bar{\omega})k_s' l_s$$

$$+ (\omega_i - \bar{\omega})k_i' l_i - (\omega_s + \omega_i - 2\bar{\omega})k_p' l_p]$$

$$+ [\tfrac{1}{2}(\omega_s - \bar{\omega})^2 k_s'' l_s + \tfrac{1}{2}(\omega_i - \bar{\omega})^2 k_i'' l_i$$

$$- \tfrac{1}{2}(\omega_s + \omega_i - 2\bar{\omega})^2 k_p'' l_p], \quad \text{(B1)}$$

where $k_{s,i}' \equiv \partial k_{s,i}/\partial\omega|_{\bar{\omega}}$, $k_p' \equiv \partial k_p/\partial\omega|_{2\bar{\omega}}$, $k_{s,i}'' \equiv \partial^2 k_{s,i}/\partial\omega^2|_{\bar{\omega}}$, and $k_p'' \equiv \partial^2 k_p/\partial\omega^2|_{2\bar{\omega}}$. The first bracketed term depends only on the mean frequency of the downconversion, and not on the particular signal and idler frequencies which are detected. The second and third terms, however, exhibit linear and quadratic frequency dependence. Labeling these terms as $\theta^{(0)}$, $\theta^{(1)}$, and $\theta^{(2)}$, respectively, we may write

$$\theta(\omega_s, \omega_i) = \theta^{(0)} + \theta^{(1)}(\omega_s, \omega_i) + \theta^{(2)}(\omega_s, \omega_i). \quad \text{(B2)}$$

To determine whether the frequency-independent phase approximation $\theta \cong \theta^{(0)}$ is valid, we must investigate the relative magnitudes of these terms.

Starting from the center of the crystal, a phase difference accumulates as the signal, idler, and pump beams traverse their respective paths in the two arms of the interferometer, including propagation through dispersive media (see Fig. 9). Due to the polarization rotation induced by the $\lambda/4$ plate, the signal and idler beams each spend half their time in the interferometer with o polarization and half their time with e polarization. The zero-order phase difference for the beams returning to the center of the crystal is therefore

$$\theta^{(0)} = k_o(\bar{\omega})l_o + k_e(\bar{\omega})l_e - k_p(2\bar{\omega})l_p + \frac{\bar{\omega}}{c}(L_o + L_e - 2L_p). \quad \text{(B3)}$$

The first three terms in Eq. (B3) represent the accumulated phase difference within the various dispersive elements: the BBO downconversion crystal (5 mm), the fused silica dichroic mirror (6.35 mm) at a 45° angle, and the BK-7 glass
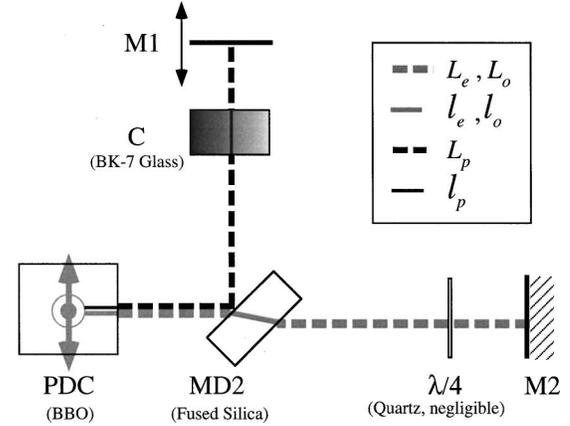

FIG. 9. The signal and idler photon pairs accumulate a frequency-dependent phase shift relative to the pump pulse as each color travels differently through dispersive elements in the Michelson interferometer. Free-space paths are indicated by thick, dashed lines, and paths inside dispersive media are indicated by thin, solid lines. Dark lines indicate the pump path; light lines indicate the signal and idler paths. Optical elements and path lengths are not drawn to scale.

slide (1.58 mm).[6] The free-space propagation lengths for the o and e downconversion beams are labeled L_e and L_o, and are identical and fixed; the free-space length for the pump L_p depends on the position of the pump mirror M1. We see that if L_p is changed by a length ΔL, the resulting change in $\theta^{(0)}$ will be

$$\Delta\theta^{(0)} = \Delta L \frac{2\bar{\omega}}{c} = 2\pi\frac{\Delta L}{\bar{\lambda}_p}. \quad \text{(B4)}$$

We therefore expect the interference fringes in the coincidence and single-channel counting rates to be governed by the mean pump wavelength $\bar{\lambda}_p = 405$ nm.

The first-order phase difference may be written as

$$\theta^{(1)}(\omega_o, \omega_e) = (\omega_o + \omega_e - 2\bar{\omega})\theta', \quad \text{(B5)}$$

where θ' is not a phase, but is a frequency-independent coefficient:

$$\theta' = \tfrac{1}{2}(k_o' l_o + k_e' l_e - 2k_p' l_p) + \frac{1}{2c}(L_o + L_e - 2L_p), \quad \text{(B6)}$$

where $k_{o,e,p}'$ now refer to the inverse group velocities within all the various dispersive media in the interferometer. For an appropriate choice of L_p, θ' can become zero, eliminating all of the first-order frequency dependence in θ. This is equivalent to balancing the path lengths in the interferometer to within the coherence length of the pump. Averaged over the range of pump frequencies $\omega_o + \omega_e$, the change in $\theta^{(1)}$ due to a change in L_p by a length ΔL is

_____

[6]The $\lambda/4$ plate is expected to contribute a negligible amount of dispersion and is omitted from these calculations.

$$\langle \Delta \theta^{(1)} \rangle_{\omega_o + \omega_e} = \frac{\langle \omega_o + \omega_e - 2\bar{\omega} \rangle_{\omega_o + \omega_e}}{2c} \Delta L = 2\pi \frac{\Delta L}{\mathcal{L}_p},$$

(B7)

where $\mathcal{L}_p = 2\pi(c/\sigma)$ is the coherence length of the pump pulse (about 50 μm).

After similar simplifications, the second-order phase difference may be written as

$$\theta^{(2)}(\omega_o, \omega_e) = [(\omega_o - \bar{\omega})^2 + (\omega_e - \bar{\omega})^2] \theta''_{oe}$$
$$- (\omega_o + \omega_e - 2\bar{\omega})^2 \theta''_p$$

(B8)

with

$$\theta''_{oe} = \frac{1}{4}(k''_o l_o + k''_e l_e),$$

$$\theta''_p = \frac{K''_p l_p}{2},$$

(B9)

where $k''_{o,e} \equiv \partial^2 k_{o,e}/\partial \omega^2|_{\bar{\omega}}$ and $k''_p \equiv \partial^2 k_e/\partial \omega^2|_{2\bar{\omega}}$ are the group velocity dispersions for each of the various media; the products $k''l$ are understood to be summed over the path lengths traveled within these media. Again, the parameters θ''_{oe} and θ''_p are not phases, but are coefficients which repre-

sent the total group velocity dispersion for the downconversion and pump pulses, respectively.

Unfortunately, no values of θ''_{oe} and θ''_p can be chosen that will entirely eliminate $\theta^{(2)}$ for all frequencies; however, we can choose values that minimize Eq. (B8) for the most likely downconversion frequencies in our experiment. To do this, we note that the most likely pairs of frequencies are those which maximize $\Phi(\omega_o, \omega_e)$ by zeroing the argument of the sinc function in Eq. (13):

$$(k'_0 - k'_p)(\omega_o - \bar{\omega}) + (k'_e - k'_p)(\omega_e - \bar{\omega}) = 0. \quad \text{(B10)}$$

This expression can be used to eliminate ω_o or ω_e in Eq. (B8): it is then possible to choose θ''_{oe} and θ''_p such that the remaining frequency dependence is zero. For our interferometer,[7] this calculation revealed that $\theta^{(2)}$ could be minimized by placing 2.04 mm of BK-7 glass into the pump arm. The plate C had an actual thickness of 1.58 mm, which left some residual quadratic dispersion uncompensated in the experiment.

To see the effects of any residual first-order dispersion (path-length imbalance) and second-order dispersion, we need only replace our original parameter θ by its expansion (B2) in the quantum state (9) and recompute the quantities of interest. For coincidence counts, the result is

$$R_{AB}(\delta\tau, \theta^{(0)}, \theta', \theta''_{oe}, \theta''_p) = R_{AB0} \left(\frac{1}{2} + \left[\frac{\tau_-}{2\sqrt{2}Z} \right] \left| \left(\frac{i}{\theta''_{oe}} \right)^{1/2} (I_0^+ + I_1^+ + I_0^- + I_1^-) \right| \cos\left\{ \theta^{(0)} + \arg\left[\left(\frac{i}{\theta''_{oe}} \right)^{1/2} (I_0^+ + I_1^+ + I_0^- + I_1^-) \right] \right\} \right.$$

$$- \left[\frac{\tau_-}{2\sqrt{2\pi}} \right] \left| \frac{I_2}{\sqrt{\theta''_{oe}[\sigma^2(2\theta''_p - \theta''_{oe}) - 4i]}} \right| \cos\left[\theta^{(0)} + \arg\left(\frac{I_2}{\sqrt{\theta''_{oe}[\sigma^2(2\theta''_p - \theta''_{oe}) - 4i]}} \right) \right]$$

$$\left. - \frac{\sqrt{\pi}}{Z} \text{erf}\left[\frac{Z}{2}\left(\frac{1}{2} - \frac{|\delta\tau|}{\tau_-} \right) \right] \text{rect}\left(\delta\tau; \frac{-\tau_-}{2}, \frac{\tau_-}{2} \right) \right),$$

(B11)

where

$$I_{0,1}^{\pm} \equiv \int_{0,1}^{1 \pm (2\theta'/\tau_o + \tau_e)} dx \exp\left(-i\frac{(\tau_- x)^2}{8\theta''_{oe}} \right) \text{erf}\left(\frac{|(\tau_o + \tau_e)(1 - x) \pm 2\theta'|}{2\sqrt{\frac{8}{\sigma^2} + 2i(2\theta''_p - \theta''_{oe})}} \right)$$

(B12)

and

$$I_2 = \int_{-1}^{1} dx(1 - |x|) \exp\left(-i\frac{\left[\frac{\tau_-}{2}x - \delta\tau \right]^2}{2\theta''_{oe}} - \frac{\left[\sigma\left(\frac{\tau_o + \tau_e}{2}x - \theta' \right) \right]^2}{8 + 2i\sigma^2(2\theta_p - \theta''_{oe})} \right).$$

(B13)

---

[7] 5-mm BBO crystal, 0.25-in. fused silica dichroic (oriented at 45° for an effective length 7.27 mm).
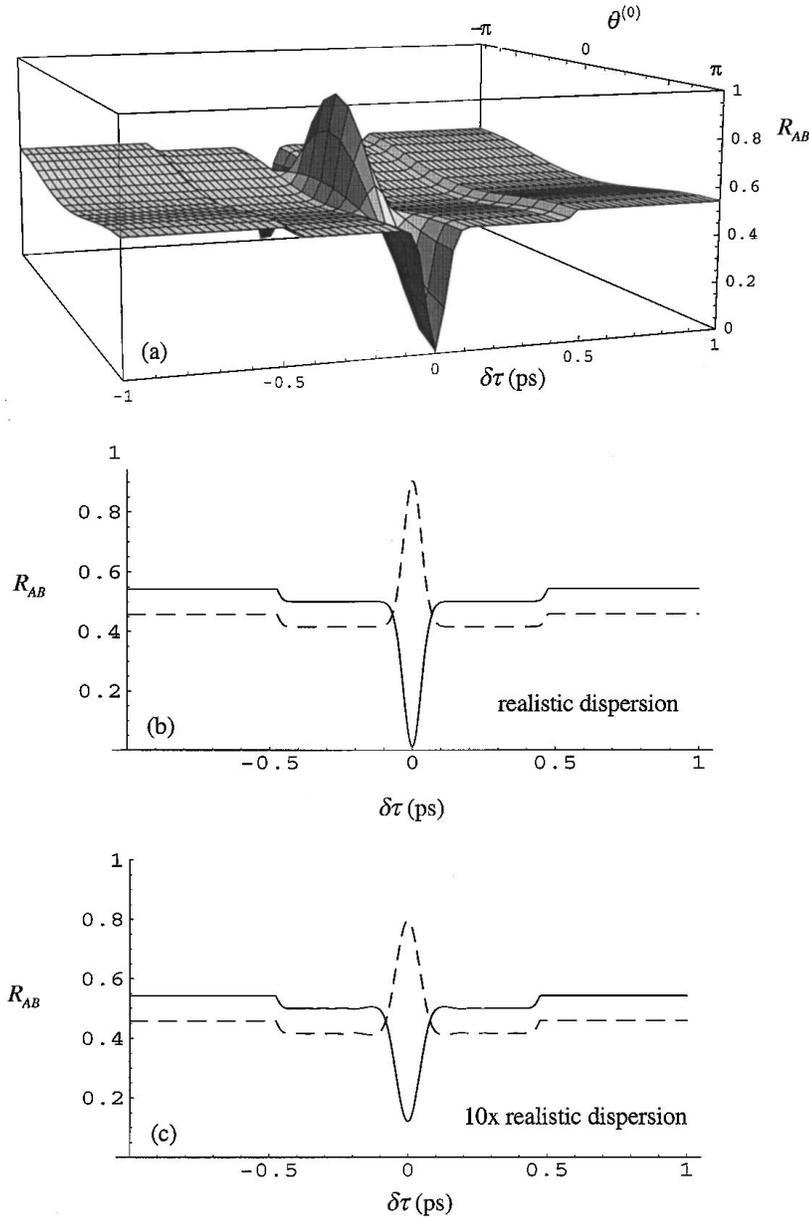
FIG. 10. (a) With dispersion in θ included, the coincidence rate $R_{AB}(\delta\tau, \theta', \theta''_{oe}, \theta''_p)$ still displays sinusoidal variation with the zero order, frequency-independent phase $\theta^{(0)}$. (b) For the symmetric case $\theta^{(0)} = 0$ (solid line), the dip is wider than before, and does not fall to zero. These plots were made with parameters corresponding to a 5-mm-long BBO crystal and a 1.58-mm-thick BK-7 glass compensator plate C: $\sigma = 34.5$ ps^{-1}, $\tau_o = 0.38$ ps, $\tau_e = 1.33$ ps, $\theta' = 0$, $\theta''_{oe} = 2.95 \times 10^{-4}$ ps^2, and $\theta''_p = 7.42 \times 10^{-4}$ ps^2. (c) The effects of dispersion in the PDC were exaggerated for this plot, by multiplying the values of θ''_{oe} and θ''_p by a factor of 10.

R_{AB0} remains as defined in Eq. (26). The integrals $I^{\pm}_{0,1}$ and I_2 must be evaluated numerically. A comparison with Eq. (25) reveals many similarities for the cases with and without dispersion: the first and last terms in the expression are unchanged, since they do not depend on θ, while the second and third terms generate fringes as θ is varied. Recalling Eqs. (B4) and (B7), and assuming

$$\mathcal{L}_p \gg \bar{\lambda}_p, \tag{B14}$$

we can regard small changes in L_p (on the order of $\bar{\lambda}_p$) as affecting $\theta^{(0)}$, but not θ'. The factors

$$\arg\left(\frac{I_2}{\sqrt{\theta''_{oe}[\sigma^2(2\theta''_p - \theta''_{oe}) - 4i]}}\right)$$

and

$$\arg\left(\frac{I_2}{\sqrt{\theta''_{oe}[\sigma^2(2\theta''_p - \theta''_{oe}) - 4i]}}\right)$$

then appear as fixed phase offsets for the new interference fringes. The new expected coincidence rate is plotted in Fig. 10(a) as $\delta\tau$ and $\theta^{(0)}$ are varied. For these plots the integrals (B12) and (B13) were computed numerically, with the assumption that the interferometer was perfectly balanced so that $\theta' = 0$, and with values of θ''_{oe} and θ''_p appropriate for the dispersion introduced by the optical elements in the experiment. Figure 10(b) is the same plot for only the values $\theta^{(0)} = 0$ and $\theta^{(0)} = \pi$; this is to be compared with Fig. 10(c), in which the dispersion has been exaggerated by a factor of 10.

We should also note what happens to this structure if the path lengths in the interferometer are out of balance by an amount comparable to the 50-μm coherence length of the
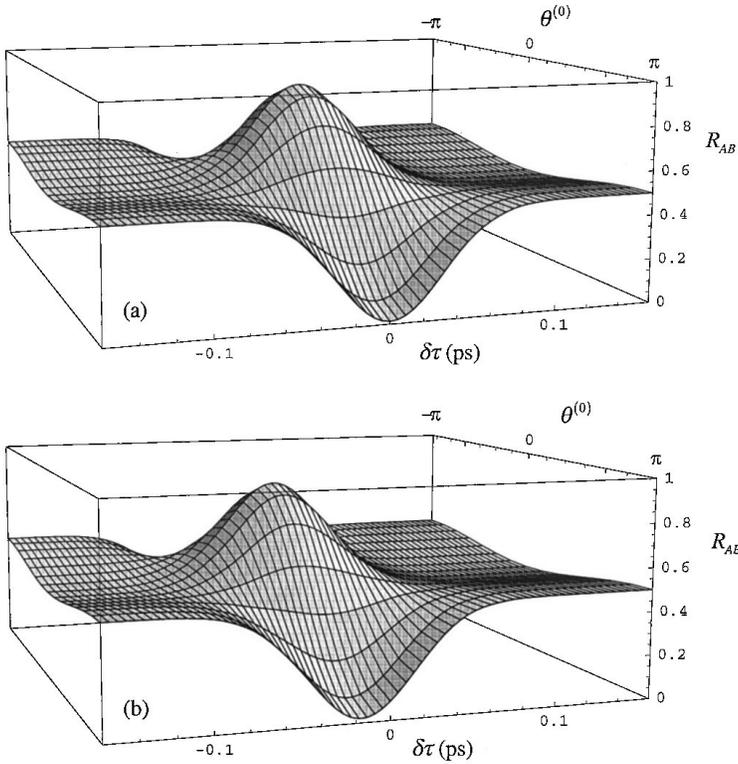
FIG. 11. (a) A blowup of the central region of the plot in Fig. 10(a); this is also Fig. 5(b) seen from a different perspective, and corresponds to the region covered by our data set. (b) The effects of a -10-μm shift in L_p. In this case, the Michelson interferometer is not balanced, and the first-order dispersion term (nominally zero) has a value of $\theta' = -0.033$ ps. There is a shift in the position of the dip away from $\delta\tau = 0$, and a slight reduction in visibility.

pump. In this situation, the first-order dispersion coefficient θ' is no longer zero. In fact, the alignment procedure in the actual experiment may have allowed the pump mirror M1 to be offset from the optimal path length balancing condition by as much as 10 μm. The effect of such an error is shown in Fig. 11: the net result is a translation of the central dip and peak structures away from $\delta\tau = 0$ and a slight reduction in the dip visibility.

We can understand these effects by considering the events shown in Fig. 12(c), but this figure is clearer if we first consider Fig. 12(a) and 12(b). Figure 12(a) depicts a cw-pumped collinear HOM interferometer, in which the top detector fires first and the bottom detector fires at a later time separated by Δt. In practice, we integrate over all possible separations, $-\tau_-/2 < \Delta t < \tau_-/2$, to obtain the measured coincidence rate, but in principle, each time separation constitutes a distinct joint detection event for which there are two possible causes: either a y photon follows an x photon (top line) or an x photon follows a y photon (bottom line). Before the quartz delay, which slows the y photon relative to the x photon by a time $\tau_-/2 + \delta\tau$, these two sets of photons must have had relative delays $\tau_-/2 + \delta\tau + \Delta t$ and $\tau_-/2 + \delta\tau - \Delta t$, respectively. In order to have acquired these different relative delays, the photon pairs must have originated from two different regions of the PDC crystal; however, they can still interfere because the continuous-wave pump does not provide any distinguishing information as to the time of origin for the photons. We can also see from Fig. 12(a) that for some of the possible separations Δt, only one of the two processes can occur—if Δt is too large, the other creation point corresponds to a point outside the crystal. This means that some fraction of the total detection events (integrated over Δt) does not participate in the destructive HOM inter-

ference; as $|\delta\tau|$ is increased from zero to $\tau_-/2$, this fraction grows linearly from zero to one, producing the familiar triangle-shaped dip in the coincidence rate R.

A pulsed-pump situation is shown in Fig. 12(b). Once again, by the previous argument, the interfering photon pairs must have been born in two different regions of the crystal. But now, the two photons carry "spectral labels," e and o, that render them somewhat distinguishable: in many cases it will be possible to tell which process actually created the detected photons by noting which frequency arrived at which detector. Alternatively, we can see that the pairs are distinguishable in the time domain, because the pump pulse will follow the first detected photon by different times for each, and could *in principle* be registered at the same pair of detectors after traveling through the same length of quartz delay.[8] In the top process, the first photon detected is the e photon; the pump pulse will lag by

$$t_{P2} - t_{e2} = \frac{\tau_e}{\tau_-}\left(\frac{\tau_-}{2} + \delta\tau + \Delta t\right) + T_P(\delta\tau)$$
$$- \left[T_o(\delta\tau) + \left(\frac{\tau_-}{2} + \delta\tau\right)\right]. \quad (B15)$$

---

[8] The pump pulse could also be detected any number of other ways, in principle, with or without having traveled through the quartz delay. We choose this particular scheme as a matter of convenience. Of course arguments about *in-principle* information should not depend on this choice, and that is the case here: if any delay were added to the optical path of the pump pulse, it would be subtracted out in Eqs. (B17) and (B20).
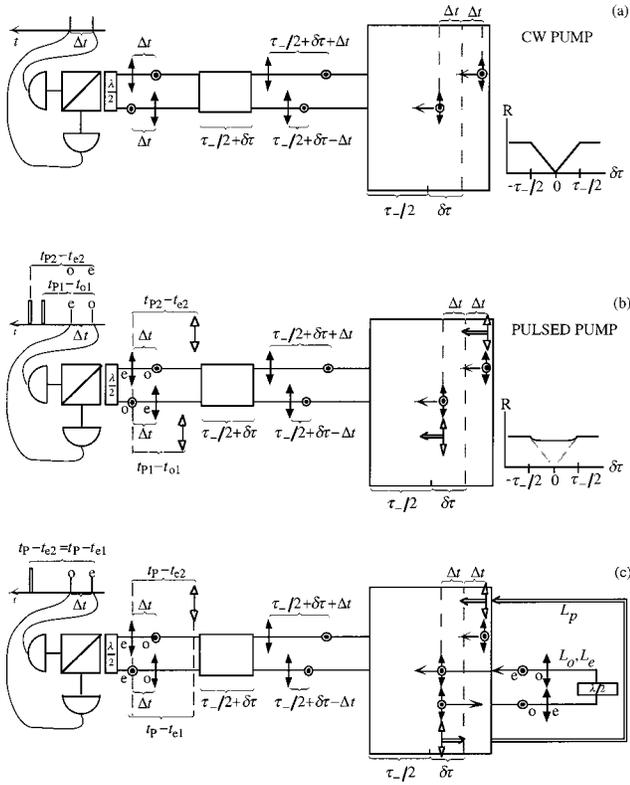
FIG. 12. (a) Collinear HOM interference with a cw pump. Two distinct pair-creation processes can give rise to photodetections separated by Δt: these are displayed on the top and bottom horizontal lines. From the amount of quartz delay present in the system, we can infer where each pair must have been born in the PDC. For some values of $\delta\tau$, one of the two sets of photons will be missing, and this occurs for a greater fraction of all the possible delays as $|\delta\tau|$ is increased: the triangle-shaped dip is the result. (b) With a pulsed pump, the signal and idler photons carry ''e'' and ''o'' spectral labels, and it is possible to distinguish which process created the pair by examining their frequencies, or by noting the lag in the arrival time of the pump pulse. This transforms the triangle-shaped dip into a trough. (c) Our experiment, in which the photons and the pump pulse from the first process are sent back through the PDC for a second pass. The spectral labels no longer convey any ''which process'' information, and with L_p adjusted correctly, the pump pulse lags the e photon by the same amount for both processes. The result is a restored interference dip, as shown in Fig. 3(b) [or Fig. 10(b) with dispersion included].

The first term corresponds to delay accumulated inside the PDC. $T_P(\delta\tau)$ and $T_o(\delta\tau)$ are the propagation times for the pump and the o photon through the quartz, and we must add to this the delay $\tau_-/2 + \delta\tau$ to get the e photon's propagation time through the quartz. In the bottom process, the first photon detected is the o photon; the pump pulse will lag by

$$t_{P1} - t_{o1} = \frac{\tau_e}{\tau_-}\left(\frac{\tau_-}{2} + \delta\tau - \Delta t\right) - \left(\frac{\tau_-}{2} + \delta\tau - \Delta t\right)$$

$$+ T_P(\delta\tau) - T_o(\delta\tau). \qquad (B16)$$

The first two terms represent the delay between the pump and the o photon accumulated in the PDC; the first term is

the delay between the pump and the e photon in the PDC; the second term then subtracts from this the walkoff between the e photon and the o photon. The final two terms again represent the delay accumulated in the quartz. The difference between the arrival delays (B15) and (B16) is

$$(t_{P2} - t_{e2}) - (t_{P1} - t_{o1}) = \Delta t\left(\frac{\tau_o + \tau_e}{\tau_-}\right), \qquad (B17)$$

which is independent of $\delta\tau$. When this quantity exceeds the temporal duration of the pump pulse, roughly $1/\sigma$, the two processes are distinguishable from each other and cannot interfere. Therefore, for every setting of the quartz delay $\delta\tau$, only those photons that arrive at the detectors with relative delays on the order of

$$\Delta t \leq \left(\frac{\tau_-}{\tau_o + \tau_e}\right)\frac{1}{\sigma} \qquad (B18)$$

can participate in the destructive HOM interference. This represents a small fraction, on the order of $1/\sigma(\tau_o + \tau_e)$, of the total number of photon pairs collected over all possible delays $-\tau_-/2 < \Delta t < \tau_-/2$. Because the destructive interference only occurs for this small fraction of the events regardless of $\delta\tau$, a flattened ''trough'' structure emerges instead of the usual triangular-shaped dip.

Our solution to this problem is depicted in Fig. 12(c), with the pair created on the bottom being reflected back into the crystal, along with the pump pulse. Again, following the logic of the first two figures, we see that the two photon pairs capable of registering with a final detection separation Δt must have originated at different points in the crystal. But now, because the e and o spectral labels have been switched for the bottom process, it is impossible to use the frequencies to determine whether the x or y photon registered at either detector. To maintain the indistinguishability of these two processes, we must arrange for the pump pulse to lag the first detected (e-polarized) photon by the same amount in each case. For the top process, this lag is again given by Eq. (B15). For the bottom process, the lag is

$$t_{P1} - t_{e1} = \frac{\tau_e}{\tau_-}\left(\frac{\tau_-}{2} - \delta\tau + \Delta t\right) + \frac{L_P - L_e}{c} + \tau_o$$

$$+ T_P(\delta\tau) - T_o(\delta\tau). \qquad (B19)$$

The first term is the delay accumulated upon passing out of the PDC; the next term is the delay accumulated during free-space propagation through the Michelson interferometer; the third term is the delay accumulated during the second pass through the length of the PDC (where the photon with the e-spectral label now propagates with the o polarization); and the final two terms represent the delay due to the quartz plates. The difference between the delays (B15) and (B19) is

$$(t_{P1} - t_{e1}) - (t_{P2} - t_{e2}) = \frac{L_P - L_e}{c} + \left(\delta\tau - \frac{\tau_-}{2}\right)\left(\frac{\tau_e + \tau_o}{\tau_-}\right).$$

$$(B20)$$

This quantity must be made zero for the two processes shown in Fig. 12(c) to be indistinguishable; in the experiment, this is achieved by positioning the pump mirror $M2$ to select the correct value of L_p. Because the quantity (B20) is independent of Δt, the same fixed value of L_p serves to maintain the indistinguishability for all of the various relative photodetection separations. However, we see that this value of L_p must be chosen for a particular value of the quartz delay—ideally, for $\delta\tau = 0$. As $\delta\tau$ is then varied, the top and bottom processes become distinguishable when the quantity (B20) exceeds the duration of the pump pulse $1/\sigma$. This accounts for the narrow width of the restored HOM dip in our experiment. Conversely, if the pump mirror is displaced so that L_p is no longer the appropriate value for $\delta\tau = 0$, there will be some new $\delta\tau$ for which L_p is, in fact, the appropriate value to make Eq. (B20) equal zero: thus, a narrow dip will appear that is centered at this new value of $\delta\tau$. This is the shift that is illustrated in Fig. 11(b).

[1] J. A. Wheeler and W. H. Zurek, *Quantum Theory and Measurement*, Princeton Series in Physics, edited by A. S. Wightman and P. W. Anderson (Princeton University Press, Princeton, NJ, 1983).

[2] L. Mandel, in *More Things in Heaven and Earth: A Celebration of Physics at the Millennium*, edited by B. Bederson (Springer-Verlag, New York, 1999), p. 460.

[3] A. Zeilinger, in *More Things in Heaven and Earth: A Celebration of Physics at the Millennium* (Ref. [2]), p. 482.

[4] A. Aspect, J. Dalibard, and G. Roger, Phys. Rev. Lett. **49**, 1804 (1982).

[5] Y. H. Shih and C. O. Alley, Phys. Rev. Lett. **61**, 2921 (1988).

[6] Z. Y. Ou and L. Mandel, Phys. Rev. Lett. **61**, 50 (1988).

[7] G. J. Milburn, *The Feynman Processor* (Perseus Books, Reading, MA, 1998).

[8] A. Migdall, Phys. Today **52 (1)**, 41 (1999).

[9] L. Mandel and E. Wolf, *Optical Coherence and Quantum Optics* (Cambridge University Press, Cambridge, 1995).

[10] P. G. Kwiat *et al.*, Phys. Rev. Lett. **75**, 4337 (1995).

[11] P. G. Kwiat *et al.*, Phys. Rev. A **60**, R773 (1999).

[12] R. P. Feynman, R. B. Leighton, and M. Sands, *The Feynman Lectures on Physics* (Addison-Wesley, Reading, 1965).

[13] C. K. Hong, Z. Y. Ou, and L. Mandel, Phys. Rev. Lett. **59**, 2044 (1987).

[14] D. Bouwmeester *et al.*, Nature (London) **390**, 575 (1997).

[15] J. W. Pan, D. Bouwmeester, H. Weinfurter, and A. Zeilinger, Phys. Rev. Lett. **80**, 3891 (1998).

[16] D. Bouwmeester *et al.*, Phys. Rev. Lett. **82**, 1345 (1999).

[17] A. Zeilinger, Phys. World **11**, 35 (1998).

[18] J. Paye, IEEE J. Quantum Electron. **28**, 2262 (1992).

[19] W. P. Grice and I. A. Walmsley, Phys. Rev. A **56**, 1627 (1997).

[20] T. E. Keller and M. H. Rubin, Phys. Rev. A **56**, 1534 (1997).

[21] G. Di Giuseppe, L. Haiberger, F. De Martini, and A. V. Sergienko, Phys. Rev. A **56**, R21 (1997).

[22] W. P. Grice, R. Erdmann, I. A. Walmsley, and D. Branning, Phys. Rev. A **57**, R2289 (1998).

[23] D. Branning, W. P. Grice, R. Erdmann, and I. A. Walmsley, Phys. Rev. Lett. **83**, 955 (1999).

[24] C. K. Law, I. A. Walmsley, and J. H. Eberly, Phys. Rev. Lett. (to be published).

[25] L. Mandel, Opt. Lett. **16**, 1882 (1991).

[26] Y. H. Shih and A. V. Sergienko, Phys. Lett. A **191**, 201 (1994).

[27] T. J. Herzog, J. G. Rarity, H. Weinfurter, and A. Zeilinger, Phys. Rev. Lett. **72**, 629 (1994).

[28] H. Weinfurter *et al.*, in *Fundamental Problems in Quantum Theory: A Conference Held in Honor of Professor John A. Wheeler*, edited by D. M. Greenberger and A. Zeilinger (New York Academy of Sciences, New York, 1995), Vol. 755, p. 61.

[29] T. J. Herzog, P. G. Kwiat, H. Weinfurter, and A. Zeilinger, Phys. Rev. Lett. **75**, 3034 (1995).

[30] T. P. Grayson and G. A. Barbosa, Phys. Rev. A **49**, 2948 (1994).

[31] M. Atatüre *et al.*, Phys. Rev. Lett. **83**, 1323 (1999).